Published by IOP Publishing for Sissa Medialab

Received: *October 14, 2019*
Revised: *December 11, 2019*
Accepted: *January 4, 2020*
Published: *February 18, 2020*

21st International Workshop on Radiation Imaging Detectors
7–12 July 2019
Crete, Greece

Characterization of SINTEF 3D diodes with trenched-electrode geometry before and after neutron irradiation

R. Mendicino,[a,1] **A. Kok,**[c] **O. Koybasi,**[c] **M. Povoli,**[c] **A. Summanwar**[c] **and G.-F. Dalla Betta**[a,b]

[a] *TIFPA INFN, Via Sommarive 14, Trento 38123, Italy*
[b] *Dipartimento di Ingegneria Industriale, Università di Trento, Via Sommarive 9, Trento 38123, Italy*
[c] *SINTEF MiNaLab, Gaustadallen 23C, Oslo 0373, Norway*

E-mail: roberto.mendicino@unitn.it

Abstract: We report on the characterization of 3D diodes with trenched electrodes and active edges manufactured by SINTEF MiNaLab (Oslo, Norway), and irradiated with reactor neutrons up to a maximum fluence of $2 \times 10^{16}\,n_{eq}\,cm^{-2}$. The charge collection performance of these test structures is investigated by using a position resolved pulsed laser system, and discussed with the aid of TCAD simulations. In spite of the non-idealities of the test setup, whose spatial resolution is not fine enough for the small-pitch geometries of the considered samples, results confirm the good radiation hardness of 3D sensors with trenched electrodes.

Keywords: Radiation damage to detector materials (solid state); Radiation-hard detectors

[1] Corresponding author.

https://doi.org/10.1088/1748-0221/15/02/C02023

Contents

2020 JINST 15 C02023

1 Introduction

Among sensors with high radiation tolerance and high time resolution, which are of interest for charged particle detection in High Energy Physics (HEP) and space applications, 3D silicon sensors have become increasingly popular for their outstanding properties. First introduced by S. Parker in the mid 90' [1], 3D sensors exploit the reduced distance between vertical electrodes of opposite doping type to yield excellent performance in terms of high radiation hardness at relatively low bias voltage (hence low power dissipation) [2]–[7]. As a result, they currently represent the most promising option for the innermost layers of tracking detectors at the High Luminosity LHC (HL-LHC).

A limit to 3D sensor performance comes from the spatial non-uniformity of the electric field and weighting field [8], that translates into a non-uniform charge collection efficiency after high radiation fluences and also represents the most significant drawback for timing applications [9]. Different design solutions are possible to improve 3D sensors from this stand-point by using modified layout and electrode geometries. Among them, 3D sensors with trenched-electrodes promise to yield the best results, according to TCAD device simulations, so that dedicated efforts have been started to develop this type of 3D sensors [10]–[12].

SINTEF MiNaLab has a long experience in 3D detectors aimed at different applications, from HEP to space science, from neutron detection to radiation monitoring and dosimetry, and is currently involved in the development of small-pitch 3D pixel sensors for the HL-LHC detector upgrades [13]. In the framework of its recent R&D programs on 3D detectors, SINTEF has fabricated prototypes of 3D diodes with trenched electrodes and active edges, that are the object of this study.

In this paper, we report results of position resolved laser tests performed on 3D diodes with trenched electrodes before irradiation and after irradiation with reactor neutrons up to a very large fluence of 2×10^{16} n_{eq} cm^{-2}, which represents the worst-case scenario for pixels at the HL-LHC. The remaining part of the paper is organised as follows: section 2 will describe the devices, the irradiation, and the measurement setup. In section 3, experimental results and TCAD simulations are reported and discussed. Conclusion follows in section 4.

2 Devices under test and measurement setup

In this study, we have used 3D sensors fabricated at SINTEF MiNaLab, Oslo, Norway. Devices were fabricated in Si-Si Direct Wafer Bonded (DWB) substrates with a high-resistivity ($6-12\,k\Omega\cdot cm$), p-type Float Zone wafer of 100 µm active thickness fusion bonded to a low-resistivity p-type handle wafer of 300 µm thickness.

A Scanning Electron Microscope cross-section of a device and a layout detail are shown in figure 1. The p^+ trench and n^+ trench have the same nominal lateral size of 2 µm, but different depths: while the former penetrates through the entire active layer thickness, the latter stops at ~ 25 µm distance from the support wafer. Both types of trenches are filled with doped poly-Si and are contacted by metal on the front side through highly doped regions surrounding the trench openings at the surface. The devices feature segmented parallel trenches of opposite doping type alternated along Y direction at a fixed pitch of 50 µm (p_y), with an inter-electrode distance (D) of 25 µm. Two device geometries are present which differ in the trench dimensions along X direction: the "150 × 50" variant has 150 µm pitch (p_x) and 100 µm width (w_x); the "100 × 50" variant (shown in figure 1b) has p_x=100 µm and w_x= 50 µm. The devices will be referred to using labels "150 × 50" and "100 × 50", which represent the dimensions of their basic 3D cell sizes.

All trenched-electrode segments of the same doping type are shorted on the front surface by metal interconnects ending in separate pads for bias and readout. The p^+ trenches are also shorted to the p^+ active edge. By doing so, 2-electrode devices are obtained, i.e., 3D diodes. This configuration facilitates the electrical testing with respect to pixels, but it also comes with a much higher capacitance and leakage current, hence higher noise. In order to overcome these problems, functional tests can be performed by using laser systems, which allow to average the signal over a large number of measurements, thus minimizing the impact of high noise.

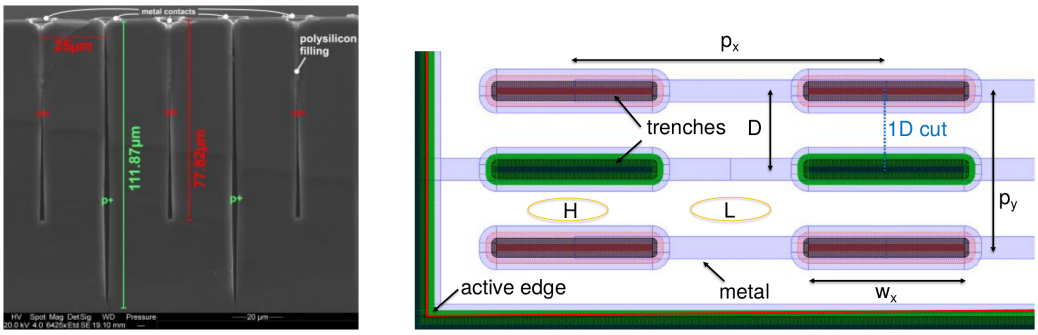

(a) **(b)**

Figure 1. a) Scanning Electron Microscope cross-section of a 3D diode with trench electrodes showing the etching depths for both types of trenches, the pitch between the trenches, the position of the metal contacts and the polysilicon filling inside the 3D electrodes; b) layout detail of a "100 × 50" diode, i.e., having 100 µm pitch (p_x) with 50 µm trench width (w_x) along X, and 50 µm pitch (p_y) along Y, corresponding to an inter-electrode distance (D) of 25 µm.

Sensors were irradiated with neutrons at the TRIGA Mark II reactor at JSI (Ljubljana, Slovenia) to three different fluences: 5×10^{15}, 1×10^{16}, and 2×10^{16} $n_{eq}\,cm^{-2}$, with 10% uncertainty [14]. No bias was applied during irradiation. All irradiated samples were stored in a freezer at −20°C to

2020 JINST 15 C02023

avoid annealing. Annealing effects at room temperature during preparation for the measurements are expected to be negligible.

The measurement setup is shown in figure 2: it consists of a laser with wavelength of 1064 nm and nominal pulse width 40 ps connected through an optical fiber to a (x, y, z) position resolved microscope and a custom vacuum chamber. A vacuum pump forces the pressure to 20 mBar that is low enough to maintain the air contained in the chamber at the gaseous phase The vacuum chamber acts as a small probe station with incorporated the first electronics stage: instead of a thermal chuck there is a thermal finger (or heat exchanger) and contact to the detector are obtained by the micromanipulators and the microneedles. A temperature sensor (PT100 RTD) placed in proximity to the 3D diodes monitors the temperature during the measurements. The chamber lid has an optical window that has a minimal light attenuation for the used wavelength. The temperature during the measurements was fixed to 255 K (−18°C).

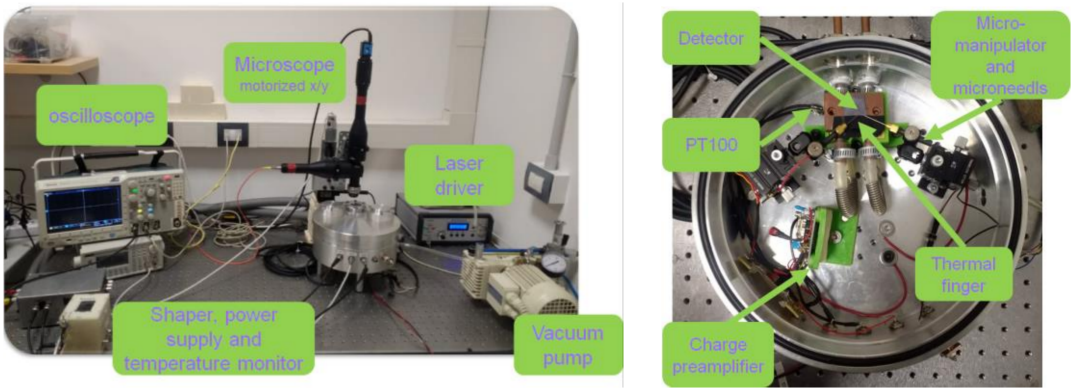

(a) **(b)**

Figure 2. a) The acquisition chain composed of: microscope, laser, oscilloscope, vacuum chamber and acquisition chain; b) detail of the vacuum chamber for the sensor testing.

The read-out electronics chain is composed by a low-noise charge preamplifier, that is placed in the chamber in order to reduce the environmental interference on the detector signal, a shaping filter with a shaping time of 4 µs, and an oscilloscope for acquiring the signal. The reverse bias voltage applied to the detector was in the range between 0 and 100 V (or until breakdown was reached), with steps of 25 V, except for the first measurements at 10 V.

The laser pulses were focused at the middle of the active layer thickness, i.e., at 50 µm depth from the front surface. The spot size is expected to be gaussian with a standard deviation of 6 µm.

The motorized microscope is controlled by a PC in both X and Y directions with a precision less than 1 µm. The step size was fixed to 5 µm in both directions, and the obtained signal maps were interpolated with a grid of 1 µm.

The efficiency calculations were performed by normalizing the signal acquired from irradiated samples to the maximum signal acquired from a non-irradiated sample in the region of interest. The normalization step is not straightforward, since it must take in account the impact of radiation on the light absorption coefficient (α). The charge $Q(\phi, \lambda, T, t_{FZ})$ generated by the laser light in the detector depends on the fluence (ϕ), the wavelength (λ), the temperature (T) and the thickness of

2020 JINST 15 C02023

the active region (t_{FZ}). According to Lambert-Beer law, it can be expressed as in eq. (2.1):

$$Q(\phi, \lambda, T, t_{FZ}) = Q_0 \cdot [1 - \exp(-\alpha(\phi, \lambda, T) \cdot t_{FZ})] \tag{2.1}$$

where Q_0 is a proportionality factor, depending on the laser intensity, that is not affected by the irradiation fluence, so as to be canceled in the signal normalization. The ratio between the released charge before and after irradiation yields a correction factor to be applied in the normalization of the signals acquired before and after irradiation. Following [15], the light absorption coefficient $\alpha(\phi, \lambda, T)$ can be calculated by using eq. (2.2):

$$\alpha(\phi, \lambda, T) = \alpha_0(\lambda, T) \cdot \left[1 + \frac{\phi}{\phi_{\text{abs}}(\lambda)}\right]. \tag{2.2}$$

The value of the absorption coefficient before irradiation $\alpha_0(\lambda, T)$ has been calculated by using the model proposed in [16] at a temperature of 255 K and λ=1064 nm. The coefficient ϕ_{abs} for the wavelength of interest has been assumed to be $3.37 \pm 0.36 \times 10^{16}$ cm^{-2} [15]. All data relevant to the signal normalization are shown in table 1. In particular, the signal efficiency has been calculated as the ratio between the signals from the irradiated sensor divided by the scaling factor and the maximum signal measured before irradiation in the region of interest of the devices.

Table 1. Summary of data relevant to 1064 nm light absorption at −18°C (255 K) and charge released in the 100 µm thick active layer before irradiation and after irradiation at different fluences. Keeping into account the uncertainties on the value of ϕ_{abs} [15], the uncertainties in the scaling factors are at most ∼ 4%.

ϕ (10^{16} n_{eq} cm^{-2})	α @ 255 K (cm^{-1})	Charge in t_{Fz} (10^{-2} Q_0)	Scaling factor
0	5.26	5.13	n.a.
0.5	6.05	5.87	1.14
1.0	6.83	6.60	1.29
2.0	8.39	8.05	1.57

3 Results and discussion

3.1 Before irradiation

Figure 3 shows the two-dimensional maps of the signal efficiency (SE) measured before irradiation of two 3D diodes at a reverse bias of 50 V.

In figure 3a, relevant to the corner region of a device of "100 × 50" type, it can be observed that the regions covered by metal (e.g., the trenched electrodes, labeled with B and C, and the frame close to the active edge) show the minimum signals, due to laser light reflection. Nevertheless, non-zero signals are observed anyway due to the relatively large size of the light spot. The region with the highest signals is the one closest to the active edge. This is due to the wider area free of metal present therein (less reflection), and to the distortion of the electric field lines due to the active edge itself [17]–[19]. In order for the signal normalization of the irradiated samples not to be affected by these anomalous values, the regions close to the active edge were not considered.

2020 JINST 15 C02023

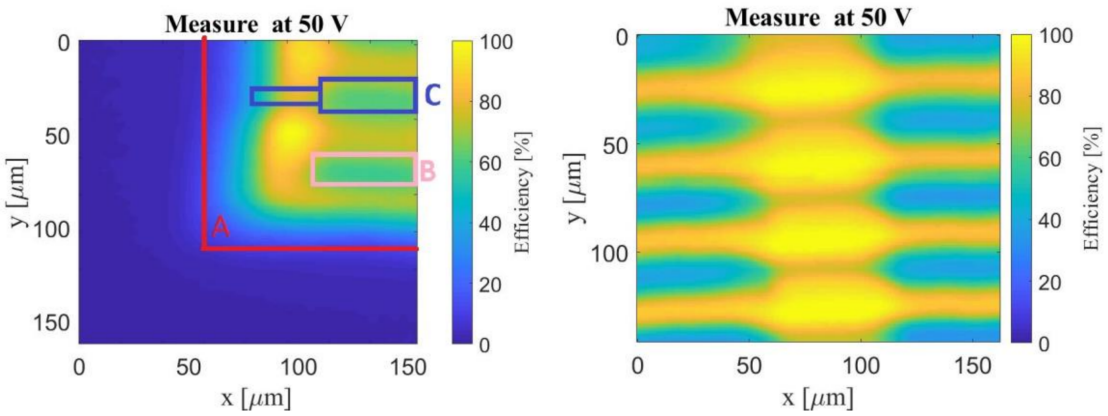

(a) (b)

Figure 3. a) Two-dimensional maps of signal efficiency measured at 50 V before irradiation: a) in the corner region of a 3D diode of "100 × 50" type, and b) in the central region of a 3D diode of "150 × 50" type. In figure 3a, the red line labeled with A represents the active edge, whereas regions labeled with B and C correspond to the metal layer covering the n^+ and p^+ trenches, respectively. Note that the signal maps are slightly rotated in the X–Y plane, because of a small tilt during the alignment phase, that is not totally under control.

As an example of other measurements taken in the central region, far from the edge, figure 3b shows the map of SE for a device of "150×50" type. The signal is high in the regions in between the trenched electrodes of opposite doping type (labeled as H — for high electric field — in figure 1b), which, before irradiation, are expected to be fully efficient. Due to the non-negligible light spot size and the reduced shielding effect from the metal, it can be seen that the signal is even higher in the regions aside along X (labeled as L — for low electric field — in figure 1b), where a wider region free of metal is present. Despite the low electric field, charge collection is fully efficient before irradiation also in this region, due to the very long recombination times and the relatively long shaping time of 4 μs. However, this is not the case after irradiation, so for the signal normalization of irradiated samples, the maximum signal values measured in region H were used.

3.2 After irradiation

Figure 4 shows two examples of signal efficiency maps in irradiated 3D diodes: figure 4a refers to a sample of "150 × 50" type, irradiated at 5×10^{15} n_{eq} cm^{-2}, biased at 75 V, whereas figure 4b refers to a device of "100 × 50" type, irradiated at 1×10^{16} n_{eq} cm^{-2}, biased at 100 V. These maps have been chosen as representative of the typical behavior observed on all irradiated samples.

The highest SE is always observed in the H regions (figure 1b), as expected, with a maximum in their central parts. From theory, as well as from previous measurements on other irradiated 3D sensors with columnar electrodes [20], it would be expected that the signals were peaked closer to the electrodes. This discrepancy depends on the two factors already mentioned above: the reflection of light from the metal covering the electrodes, which attenuates the amount of charge released close to the trenches, and the laser spot size, that is not small enough to provide the fine spatial resolution necessary for the considered geometries. Note that, besides regions covered by metal, after irradiation the SE is very small also in the L regions (figure 1b), due to the low electric

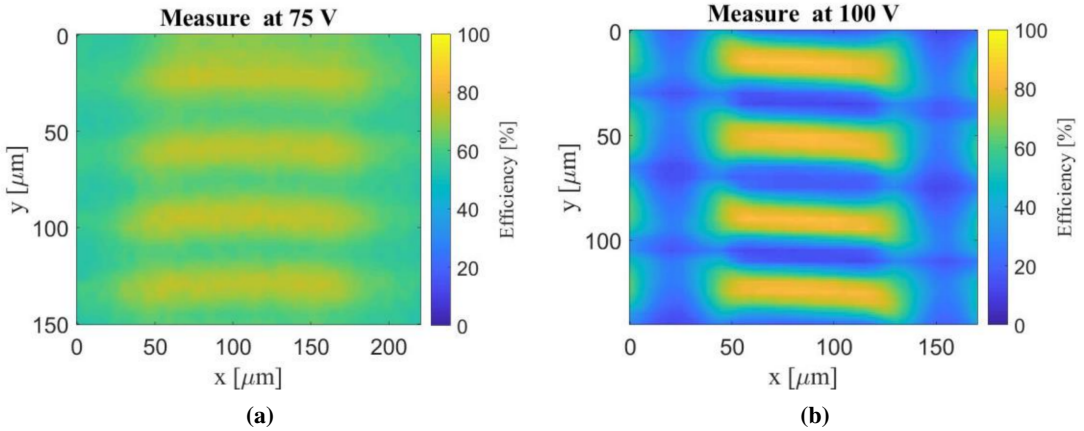

(a) (b)

Figure 4. Two-dimensional maps of signal efficiency in irradiated 3D diodes: a) device of "150 × 50" type, irradiated at 5×10^{15} n_{eq} cm^{-2}, at 75 V bias; b) device of "100 × 50" type, irradiated at 1×10^{16} n_{eq} cm^{-2}, at 100 V bias.

field. This effect becomes more pronounced as the fluence is increased (compare e.g., figure 4a and figure 4b), and can be explained by the increasing importance of charge trapping.

In order to show a more quantitative comparison between the results at different fluences, a longitudinal cut section at the center of the H regions was considered (see "D cut" in figure 1b). Note that by restricting the analysis to this cut, the differences between the two device options are negligible. The SE values along these 1D cuts in a 10 μm wide region about the signal maximum have been averaged and the results are shown in figure 5, where the error bars represent the standard deviations. Data relevant to 5×10^{15} and 2×10^{16} n_{eq} cm^{-2} fluences show the expected trend, with initial increase and saturation. On the contrary, the non-regular behavior of the device irradiated at 1×10^{16} n_{eq} cm^{-2} is still under investigation. It might be due to multiplication effects at the tips of the trenches. The maximum values of SE at the two lower fluences are relatively high, reaching ~ 70% (80%) after 5×10^{15} (1×10^{16}) n_{eq} cm^{-2}. At the highest fluence, the maximum SE is quite lower, ~ 43%, because of the limited voltage range that could be explored because of early breakdown.

In order to gain more insight into the experimental results, numerical device simulations have been performed using Synopsys Sentaurus TCAD. The simulation domain is a two-dimensional slice of the 3D basic cell along a plane orthogonal to the trenched electrodes. The 3-level "new Perugia" trap model for p-type silicon was used to account for bulk radiation damage effects [21].

As an example, figure 6a shows the simulated distribution of the electric field at 100 V reverse bias in the basic cell of a 3D diode of the "100 × 50" type irradiated at 5×10^{15} n_{eq} cm^{-2}. It can be seen that the intensity of the electric field is very high and uniform only in the H region, whereas it rapidly decreases outside. This is in good agreement with the measured signal maps: in fact, after irradiation, high signals can only be obtained from regions with high electric field and fast drift of charge carriers. Similar results were obtained for the "150 × 50" geometry and for the other values of fluence.

Signal simulations have been performed using the so-called HeavyIon model, by releasing fixed amounts of charge at different hit points along the same 1D cut shown in figure 1b, with a step of

2020 JINST 15 C02023

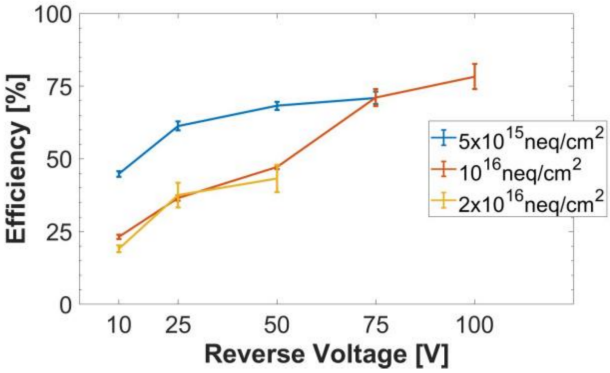

Figure 5. Signal efficiency along an interval of 10 µm at the center of the 1D cuts (see figure 1b) as a function of voltage at the three fluences. Data represent the average of the values whereas the error bars are the standard deviations.

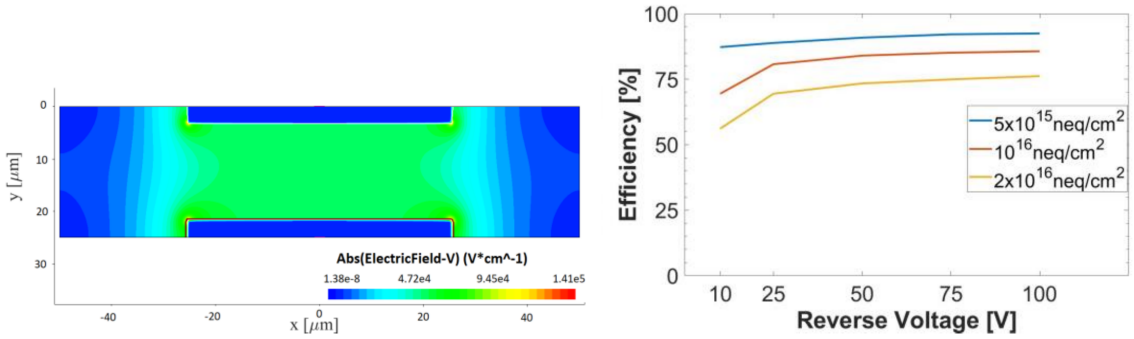

Figure 6. TCAD simulation results: a) distribution of the electric field for the basic cell of the "100 × 50" geometry, and b) simulated average signal efficiency along the 1D cut at the center of the H region at three different irradiation fluences.

1 µm and a Gaussian lateral profile of 0.25 µm width. Simulations were repeated at different values of bias voltage, namely 10, 25, 50 and 100 V, and avalanche generation model was activated. The integral of current pulses from different hit points, normalized to the charge released at each point, represents the signal efficiency. The average values are shown in figure 6b. At all fluences, the SE initially increases with voltage, and then tends to saturate, without sign of signal multiplication up to 100 V. The trend is qualitatively similar to the experimental one, but the maximum values of SE are significantly larger, reaching 92% (76%) after 5×10^{15} (2×10^{16}) $n_{eq}\,cm^{-2}$ at 100 V bias. The main reason for this discrepancy is likely to be attributed to the limited spatial resolution of the experimental setup, which prevents the regions with maximum signals close to the electrodes to be included in the average estimate of the SE. Moreover, the considered 2-d simulations do not consider the region at the bottom of the device where trenched-electrodes are not overlapping, which are more difficult to deplete and from which therefore a lower efficiency should be expected after irradiation.

4 Conclusion

We have reported on the position-resolved laser characterization of neutron irradiated 3D sensors with trenched electrodes. The two-dimensional maps of the signal efficiency are in good agreement

2020 JINST 15 C02023

with theoretical expectations and with numerical device simulations. The measured values of signal efficiency from the region of high electric field is instead found to be smaller than the one predicted by simulations. This discrepancy is mainly to be attributed to the limits in the laser system setup, whose spatial resolution is too coarse for the considered devices which have an inter-trench pitch of only 25 µm. In addition, 2-d simulations have so far been performed, whereas 3-d ones would be more appropriate to better investigate the non-idealities in the charge collection from the region at the bottom of the device where the trenches are not overlapping.

Acknowledgments

This project has received funding from the European Space Agency, Project "Three-dimensional Low-Voltage Silicon Detectors" and from the Italian National Institute for Nuclear Physics (INFN), 5th Scientific Commission (CSN5), Project TIMESPOT.

References

[1] S.I. Parker, C.J. Kenney and J. Segal, *3D: A New architecture for solid state radiation detectors*, *Nucl. Instrum. Meth.* **A 395** (1997) 328.

[2] M. Kohler et al., *Comparative measurements of highly irradiated n-in-p and p-in-n 3D silicon strip detectors*, *Nucl. Instrum. Meth.* **A 659** (2011) 272.

[3] G.-F. Dalla Betta et al., *Radiation hardness tests of double-sided 3D strip sensors with passing-through columns*, *Nucl. Instrum. Meth.* **A 765** (2014) 155.

[4] J. Lange et al., *Radiation hardness of small-pitch 3D pixel sensors up to a fluence of* $3 \times 10^{16}\ n_{eq}/cm^2$, 2018 *JINST* **13** P09009 [arXiv:1805.10208].

[5] S. Terzo et al., *Performance of Irradiated RD53A 3D Pixel Sensors*, 2019 *JINST* **14** P06005 [arXiv:1903.04838].

[6] CMS Tracker collaboration, *First Results on 3D Pixel Sensors Interconnected to the RD53A Readout Chip after Irradiation to* $1 \times 10^{16}\ n_{eq}\ cm^{-2}$, 2019 *JINST* **14** C06018 [arXiv:1903.01963].

[7] J. Duarte-Campderros et al., *Results on proton-irradiated 3D pixel sensors interconnected to RD53A readout ASIC*, *Nucl. Instrum. Meth.* **A 944** (2019) 162625.

[8] S.I. Parker et al., *Increased speed: 3D silicon sensors. Fast current amplifiers*, *IEEE Trans. Nucl. Sci.* **58** (2011) 404.

[9] G. Kramberger et al., *Timing performance of small cell 3D silicon detectors*, *Nucl. Instrum. Meth.* **A 934** (2019) 26 [arXiv:1901.02538].

[10] R. Mendicino et al., *3D trenched-electrode sensors for charged particle tracking and timing*, *Nucl. Instrum. Meth.* **A 927** (2019) 24.

[11] G.T. Forcolin et al., *Development of 3D trenched-electrode pixel sensors with improved timing performance*, 2019 *JINST* **14** C07011.

[12] A. Montalbano et al., *A systematic study of BNL's 3D-Trench Electrode detectors*, *Nucl. Instrum. Meth.* **A 765** (2014) 23.

[13] O. Dorholt et al., *Beam tests of silicon pixel 3D-sensors developed at SINTEF*, 2018 *JINST* **13** P08020 [arXiv:1806.08293].

2020 JINST 15 C02023

[14] G. Kramberger, *Signal development in irradiated silicon detectors*, Ph.D. Thesis, University of Ljubljana, Ljubljana Slovenia (2001) and online pdf version at http://www-f9.ijs.si/~gregor/papers/dok_eng.pdf.

[15] C. Scharf, *Radiation damage of highly irradiated silicon sensors*, Ph.D. Thesis, University of Hamburg, Hamburg Germany (2018) [PUBDV-2018-03707] [https://doi.org/10.3204/PUBDB-2018-03707].

[16] H.T. Nguyen, F.E. Rougieux, B. Mitchell and D. Macdonald, *Temperature dependence of the band-band absorption coefficient in crystalline silicon from photoluminescence*, *J. Appl. Phys.* **115** (2014) 043710.

[17] J. Kalliopuska, L. Tlustos, S. Eränen and T. Virolainen, *Characterization of edgeless pixel detectors coupled to Medipix2 readout chip*, *Nucl. Instrum. Meth.* **A 648** (2011) S32.

[18] R. Bates et al., *Characterisation of edgeless technologies for pixellated and strip silicon detectors with a micro-focused X-ray beam*, 2013 *JINST* **8** P01018.

[19] D. Maneuski et al., *Edge pixel response studies of edgeless silicon sensor technology for pixellated imaging detectors*, 2015 *JINST* **10** P03018.

[20] R. Mendicino, M. Boscardin and G.-F. Dalla Betta, *Characterization of FBK small-pitch 3D diodes after neutron irradiation up to* $3.5 \times 10^{16}\ n_{\mathrm{eq}}\ cm^{-2}$, 2019 *JINST* **14** C01005 [arXiv:1810.05856].

[21] F. Moscatelli et al., *Effects of Interface Donor Trap States on Isolation Properties of Detectors Operating at High-Luminosity LHC*, *IEEE Trans. Nucl. Sci.* **64** (2017) 2259.

2020 JINST 15 C02023